Halide perovskite dynamics at work: Large cations at 2D-on-3D interfaces are mobile

Sujit Kumar[a,b,c] , Lothar Houben[d] , Katya Rechav[d] , and David Cahen[a,b,c,1]

[a]Department of Molecular Chemistry and Materials Science, Weizmann Institute of Science, Rehovot-7610001, Israel; [b]Bar-Ilan Institute for Advanced Materials and Nanotechnology, Bar-Ilan University, Ramat Gan-5290002, Israel; [c]Department of Chemistry, Bar-Ilan University, Ramat Gan-5290002, Israel; and [d]Department of Chemical Research Support, Weizmann Institute of Science, Rehovot-7610001, Israel

Ultra-thin hydrophobic capping layers of two-dimensional (2D) onto three-dimensional (3D) metal halide perovskites (HaPs) are an attractive strategy for preventing ambient-induced degradation and minimizing interfacial non-idealities of 3D HaPs. However, it is not obvious in how far the unusual 3D HaP lattice dynamics affect 2D-on-3D HaP composites' stability, especially at their interface, an issue important for devices made with such composites. Using low electron–fluence, four-dimensional scanning transmission electron microscopy and nanobeam electron diffraction, we show formation of the 2D ($n = 1$) phase on top of 3D perovskite, using focused-ion beam-prepared cross-sections, under conditions that minimize radiation damage. The 2D-on-3D HaP composites were prepared by controlled gas-phase surface cation exchange of 3D MAPbI$_3$ films to form A$_2$PbI$_4$, where A = (fluoro-)phenyl-ethyl-ammonium, (F)PEA. We provide direct evidence for 2D phase formation also inside the 3D matrix, likely via A cation grain boundary diffusion, and, over time, of quasi-2D phases near the surface. These results show that the 2D/3D heterointerface is dynamic; they imply that not only small, but also large A cations, (F)PEA$^+$, migrate. Structural rearrangements, leading to quasi-2D phase formation can be followed with the electron beam, which provides hitherto unknown atomistic insights into such interfaces, needed to assess their (in)stability. Apart from directly illustrating effects of HaP lattice dynamics, our results help understanding extensive (semi)empirical data on engineering 2D-on-3D composites and provide guidance for enhancing stability of such systems. Critically, our direct observation of electron beam-induced loss of long-range periodicity defines conditions for damage-free atomic-resolution studies of HaP samples, also in device-relevant configurations.

halide perovskites | 2D/3D interface | 4D-STEM | NBED | instability

Layered perovskites, commonly known as two-dimensional (2D) perovskites because of their multiple 2D quantum confinement structures (1) consisting of alternating sheets of lead halide (PbX$_6$)$^{4-}$ octahedra (X is a halide) and organic amine layers, have recently attracted renewed attention, as they provide better moisture resistance than their 3D, APbX$_3$ analogs with small organic amine (or Cs$^+$) A$^+$ cations. The Pb-based 2D Ruddlesden-Popper halide perovskites (HaPs) are generally described by the formula A$_2$A'$_{n-1}$Pb$_n$X$_{3n+1}$, where A' are bulky/long organic amine spacer cations, e.g., phenylammonium (C$_6$H$_5$C$_2$H$_4$-), butylammonium (C$_4$H$_9$-) (2–5). Although efforts have been made to use quasi-2D HaPs (those with $n \geq 2$) as the active photoabsorber for photovoltaics, performances have been mostly limited by the poor charge conduction of the organic moieties separating the layers of lead halide octahedra (6, 7). Alternatively, 2D HaPs have been used as minor components or ultrathin interfacial layers between bulk 3D perovskite and a hole transporting layer, affecting both (radiative ←→ electrical) power conversion efficiencies (PCEs) and stabilities of devices (8–10). The improved efficiency stems from the higher bandgap of the 2D than that of the 3D HaP, which makes the 2D HaP layer not only an effective electron

blocking layer but also one that passivates interface defects that act as traps. Such passivation can be explained by the structural and chemical coherence between the HaP structures.

Despite the clear interest and significant efforts in 2D/3D HaP–based device architectures, understanding of the 2D/3D interfaces is limited, and optimization is largely empirical, followed by rationalization. Most studies on 2D/3D interfaces rely on photoluminescence (PL) and X-ray diffraction (XRD) measurements (11–13). Results of these measurements are consistent with diffusion of MA$^+$ of the 3D HaP across the hetero-interface, implying an inherent instability of these interfaces (11, 14). Such an interface instability could prove detrimental when ultrathin phase-pure 2D layers are needed to combine performance with stability.

However, direct information on these interfaces has been lacking. Knowledge of structural arrangements at these 2D/3D interfaces can help understand their instability and therefore aid in controlling it. To this end, high-resolution structural detail information of the 2D/3D interface and its transformations is needed, with transmission electron microscopy (TEM) as suitable choice, as it has already been used to capture structural characteristics of the 3D HaPs (15–17). However, already for 3D HaPs there are discrepancies between the observed electron diffraction patterns (EDPs) and those that are predicted for a perfect perovskite phase (18–20). Often, the reported diffraction pattern of, for example, MAPbI$_3$, one of the most TEM-investigated 3D HaPs, does not show (110)

Significance

Surface engineering of halide perovskites (HaPs), semiconductors with amazing optoelectronic properties, is critical to improve the performance and ambient stability of HaP-based solar cells and light emitting diodes (LEDs). Ultrathin layers of two-dimensional (2D) analogs of the three-dimensional (3D) HaPs are particularly attractive for this because of their chemical similarities but higher ambient stability. But do such 2D/3D interfaces actually last, given that ions in HaPs move readily—i.e., what happens at those interfaces on the atomic scale? A special electron microscopy, which as a bonus also reveals the true conditions for nondestructive analysis, shows that the large ions that are a necessary part of the 2D films can move into the 3D HaP, a fascinating illustration of *panta rei* in HaPs.

diffraction spots, although XRD shows reflections from the corresponding planes. An example is that of (110) reflections, Segawa et al. reported their absence in EDPs, supposedly because the associated lattice planes are weakly diffracting in organic–inorganic HaPs (21). However, it is not clear why that should be the case; it is possible to observe these reflections under measurement conditions suitable to electron beam–sensitive samples, i.e., low electron beam fluence and fast acquisition of the EDPs (22). Thus, to get atomic-scale structural information on HaPs demands those and additional specialized techniques (23, 24) and analyses, rather than the conventional TEM-based approaches that have been developed and used successfully for studying robust inorganic compounds, especially oxides.

Probing electron beam–sensitive materials to investigate interfaces at atomic scales becomes even more challenging if one side of the interface is formed by a 2D (Ruddlesden-Popper) layered HaP, where the lead halide octahedral planes are connected to each other by van der Waals forces. This is probably one reason that TEM studies on 2D HaP structures have been quite limited (25, 26); to the best of our knowledge, none have yet been reported for a large field of view of 2D/3D heterointerfaces.

Atomic-scale investigations of these interfaces especially in configurations that are relevant to photovoltaic and light-emitting devices (3D/2D) is, however, difficult, for the following reasons:

1) The atomic-resolution study of those interfaces requires the preparation of thin electron-transparent samples, which increases the possibility of damaging the atomic structure of layers. For instance, a Ga ion beam, as used in a focused ion beam (FIB) microscope to cut lamellae thinner than typically 100 nm, may cause damage by ion implantation and excessive local heating (27).

2) Acquiring structural details of the lattice arrangement at the interfaces requires high electron fluence, typically around 10^3 e$^-$/Å^2 for a better than 2-Å resolution, while the critical fluence for aliphatic or aromatic organic compounds is about 100× less (28). Such a requirement in terms of electron fluence becomes even more demanding for HaPs considering the beam-induced decomposition and subsequent losses of products, causing phase degradations into nonstochiometric HaP and PbI$_2$ phases (for MAPbI$_3$ HaP). A critical electron dose $\leq$~50 e/Å^2 has been reported to capture the pristine perovskite structure of the organic A-cation–based HaPs (22, 29). Thus, high-resolution studies on 2D/3D HaP interfaces around or below the critical electron fluence could disturb the nature of these interfaces by damaging or altering them. The excess energy that is deposited in the system by the e-beam restricts the possibility of studying the material in its state of interest, i.e., the one it has while being functional, and can also act as intermediary for interface interdiffusion. Both A-site cation and especially halide components of HaPs may be able to diffuse under external stresses such as temperature, illumination, or e-beam irradiation (30, 31). These structural rearrangements and reconstructions of and between the 2D and 3D HaPs will affect the stability of 2D/3D structures, and with it the option of using 2D HaPs as passivating buffer layers in 3D devices.

We report first TEM results on the 3D HaP, MAPbI$_3$, capped by an ultrathin film of a phenylethylammonium-based 2D lead iodide HaP, focusing on the interface between them. To minimize beam-induced radiation damage during TEM observation, we resorted to 4D scanning transmission electron microscopy (STEM) experiments (32), employing scanning nanobeam electron diffraction (NBED) over a large field of view with low electron fluence. 4D datasets $I(x, y, K_x, K_y)$

comprising diffraction patterns in reciprocal space (K_x, K_y) for each probe position (x, y) on the sample (hence the name 4D) were recorded using the EMPAD (electron microscope pixel array detector) detector (33). The simultaneously recorded real-space and momentum-space information allowed us to assess the nanoscale lattice structures and associated changes in diffraction space with simultaneous spatial resolution. Further, we used time series of NBED patterns at a 1-kHz frame rate to follow the decay of diffraction details with high temporal resolution, associated with fast structural changes on a few tens of nanometers scale.

The results show the inherent structural dynamics at the atomic scale of these 2D/3D perovskites and their interfaces. We find that the instability of layered 2D HaPs on their 3D counterparts is much more pronounced under external degrading stress, e-beam irradiation, in this case. We conclude that for such 2D/3D heterostructures, part of the 2D phase—even with a supposedly stabilizing A cation, fluoro-phenyl-ethyl-amine [(F)PEA] (34)—can diffuse into the 3D lattice, both from the free and grain boundary surfaces. These findings imply that either the 3D HaP engulfs 2D cations or that not only the small but also the large A (PEA, PEA-F) cations migrate, along with the lattice reconstruction induced by such dynamics. Such a process affects the long-term stability of a 2D HaP layer used to passivate and protect the 3D HaP, especially in devices.

Methods

Ion/electron beam exposure may substantially promote conditions for migration of A-site organic cations in 2D/3D HaP heterostructures and result in structural reconstruction, thereby complicating the ability to study these structures and their interfaces at an atomic level. Hence, the conditions during the FIB preparation of lamellae for TEM and for the TEM measurements are crucial to preserve the beam-sensitive 2D/3D HaP heterostructures in an undamaged state.

Conditions for FIB Sample Preparation and TEM Measurements. Thin TEM lamellae of the 2D/3D HaP on Si substrates were prepared with a Helios 600 Dual Beam FIB-SEM instrument (Thermo Fisher Scientific). We specifically used highly (p-) doped Si (100) as substrates for the TEM studies instead of a more device-relevant one because of a few major considerations, as will be clear from the following results of our initial experiments. The commonly used FTO substrate is relatively rough (~15-nm rms roughness) and a poor thermal conductor, possibly enhancing the beam sensitivity during FIB milling (even under cryo-conditions) because of poor dissipation of heat created by the ion beam. Therefore, we chose Si wafers as mini substrates, which are ~15× better thermal conductors [~150 versus ~10 W/(m · K)] (35, 36) than fluorine-doped tin oxide (FTO) substrates and also have a smoother surface (<1-nm rms roughness versus 10- to 15-nm rms roughness) to prepare the beam-sensitive samples for the TEM measurements. An ~80-nm protective layer was thermally evaporated using adaptive pulse carbon thread evaporation at an average (very low) sputter deposition rate of 1 nm per pulse onto the samples before FIB processing. This was done to prevent any damage that may occur in the initial phase of FIB preparation, e.g., sample heating, structural deformations, and Ga$^+$ implantation. We note that the deposition method and quality of the carbon layer is of utmost importance to minimize heating and hence to prevent sample degradation and/or diffusion of any of the layers deposited on the 2D/3D HaP or from the Ga ion beam during the FIB processing. Additional protective layers of carbon (~100 nm) and Pt (~1.5 μm) were then deposited by e- and ion beam–assisted chemical vapor deposition (CVD), respectively, inside the FIB chamber. To carry out the sample lift-out, rough trenches were made by FIB milling with a Ga ion beam of 30 keV accelerating voltage and 2.8 nA beam current. A 1.8- to 2-μm thick lamella was welded to a copper lift-out semigrid with an Omniprobe micromanipulator and was then thinned down to ~150 nm thickness at 30 kV by gradually reducing the current to 300 pA, then to 100 pA, and then to 50 pA. The final low-voltage polishing steps to reach a thickness of 60 to 80 nm were done at an accelerating voltage of 5 kV and current of 50 pA, followed by a last step at 2 kV and 30 pA current. The polished sample was then transferred to a TEM sample holder and under vacuum to the TEM.

Then, 4D STEM datasets were obtained in a double aberration–corrected Themis-Z microscope (Thermo Fisher Scientific Electron Microscopy Solutions) equipped with a high-brightness field emission gun at an acceleration voltage

of 200 kV. For the 4D STEM measurements, an electron probe with a convergence angle of 0.2 mrad was adjusted and further defocused by typically 5 to 10 μm to increase the real-space probe size to several tens of nanometers in diameter, thus reducing the electron fluence below threshold values for radiation damage. A primary beam current between 1 and 4 pA was used, resulting in a typical value of the fluence of 1 e$^-$/Å^2 per beam position. The fluence rate for a single exposure on the EMPAD detector of 1 ms is 1 e$^-$/Å^2/ms at each position in the real-space scan raster. Typically, 4D STEM datasets were acquired over a real-space raster of 128 × 128 pixels, up to 256 × 256 pixels. Thus, the cumulative electron fluence for a typical 500 nm × 500 nm frame, raster scanned with 128 × 128 pixels, is ~4 e/Å^2 (detailed calculation appears in the *SI Appendix*), well below the 50 e/Å^2 critical fluence reported to cause beam damage in these samples, as also discussed later (22, 29). We use fluence to describe electrons per unit area instead of the more conventionally used electron dose, as the energy deposited by the electrons is dependent on sample parameters such as thickness, while the fluence is a reproducible instrument quantity.

All measurements were done at room temperature to avoid thermally induced phase transformations. The samples were prepared and stored in a glovebox (<1 to 2 ppm O$_2$ and H$_2$O) from where they were removed just before FIB preparation. The samples were thoroughly sealed in an evacuated box in the glovebox before being taken out for TEM sample preparation by FIB processing. The sample was exposed to ambient condition for less than a minute before closing and pumping the C-deposition system. Even though the samples are protected from the ambient after coating with 80-nm carbon, the transfer to the FIB chamber was also done in <1 min. Once the final polishing of the lamella was finished, the samples were transferred to the TEM chamber using an evacuated box. The sample lamella was exposed to ambient for <1 min till pumping of the TEM chamber started. The time between sample preparation and TEM measurements, including FIB preparation, was typically two days, during which period samples/lamella were protected from the ambient, as described above.

Results and Discussion

Ultrathin 2D HaP via Vapor Phase Surface Cation Exchange of MAPbI₃.

The 2D/3D heterointerfaces were formed using vapor phase surface cation exchange of a thin polycrystalline film of a 3D halide perovskite, MAPbI$_3$, deposited on a high-doped Si (100) substrate. To this end, diluted organo-amine vapors, viz. PEA (phenethylamine) or FPEA (fluoro-phenethylamine), were passed in N$_2$ over the surfaces of the 3D perovskite films in a custom-built chamber, resulting in controlled growth of the 2D HaP layer on the 3D HaP surface. A schematic representation of the formation of 2D/3D HaP layers and their typical morphologies under SEM and AFM scans are shown in Fig. 1 A and B, respectively (also see *SI Appendix*, Fig. S1A). This 2D-on-3D structure forms the model heterointerface for the TEM-based studies. Optical absorbance and chemical compositional analysis of such 2D/3D layers are shown in *SI Appendix*, Figs. S1B and S2. Fig. 1C shows the PL spectra of pristine MAPbI$_3$ layers and of those treated with diluted vapors of organo-amine vapors of PEA and FPEA molecules for different time durations. As shown, the 3D to 2D transition of the top few nanometers of the MAPbI$_3$ with an ~760-nm PL peak results in additional peaks in the spectrum at ~520 nm corresponding to the formation of 2D HaP species (F)PEA$_2$PbI4 [via (F)PEA surface cation exchange]. Notably, the absence of any other additional peak in the spectrum toward the higher (than 520 nm) wavelength signals the phase purity of the 2D layer formed on 3D MAPbI$_3$ layers. The information regarding the crystalline nature of these 2D/3D HaP layers was obtained from the XRD data shown in Fig. 1 D and E. The MAPbI$_3$ thin films with surface-grown 2D layers show additional lower angle diffraction peaks associated with the larger unit cell of 2D material, apart from (110), (112), and (220) peaks at 14.1, 20.6, and 28.5 2θ values, respectively, characteristic of the tetragonal 3D HaP structure. The grazing incidence XRD in Fig. 1E shows the depth-dependence of the (00l) reflections of the 2D perovskites at 5.3° and 10.8° 2θ values, highlighting the surface conversion into 2D layered materials with preferred orientation. PEA and FPEA were chosen as organo-amines instead of the

more commonly used n-butylamine (n-BAI), as the 2D HaPs produced with PEA have been reported, from PL and XRD, to form a relatively stable interface with a 3D perovskite (11). In contrast, n-BAI–based 2D HaPs showed strong evolution of the 2D/3D interfaces with formation of R$_2$(MA)$_{n-1}$PbI$_{3n+1}$ phases with higher n ($n > 1$), i.e., a higher 3D/2D ratio (12, 13).

4D-STEM at Low Electron Fluence.

Two-dimensional maps were generated from the 4D datasets to reveal the structural characteristics. Such a map represents specific features of the lattice structure of the 2D (FPEA)/3D (MA) layers of lead iodide HaPs in diffraction space. The working principle of a typical 4D STEM experiment is schematically shown in Fig. 2. An electron beam scans across the sample lamella and a diffraction pattern is collected for each raster position; in Fig. 2 four of typically a few tens of thousands of diffraction patterns are shown for illustration. The results of a typical 4D STEM experiment, performed on a 2D/3D HaP sample (*SI Appendix*, Fig. S3 and Movie S1), show the EDPs collected for each raster probe position, which are then used to gain the real-space information of the samples, i.e., the reconstructed virtual bright-/dark-field images of the samples. A virtual bright-field image, as shown in the lower half of Fig. 3A, is obtained when mapping the intensity of the nondeflected beam as a function of the raster position. The so-called angular correlation image in the upper half of Fig. 3A is a map of a crystallographic phase; the image shows the places of occurrence of Friedel pairs of diffraction with a specific lattice period. Specifically, Fig. 3A shows from where diffraction for the base period of 0.6 nm^{-1}, corresponding to the basal plane reflections of the 2D FPEA$_2$PbI$_4$ perovskite, originates. Furthermore, no needle-like features, the presence of which is a tell-tale indication of lead iodide perovskite phase degradation into PbI$_2$, are evident in the bright-field image. Such needles were clearly visible in NBED experiments on damaged PEA$_2$PbI$_4$/MAPbI$_3$/FTO samples, with the corresponding electron diffraction pattern matching that simulated for PbI$_2$ (*SI Appendix*, Fig. S4 A–C). We identified that the deleterious degradation into PbI$_2$ is related to excessive beam damage during FIB preparation of the thin lamellae for TEM observation, as noted in *Methods*.

The bright domains in the angular correlation map (apart from the region near the Si interface, which is an artifact due to the refraction of the electron beam at the Si/HaP interface) show that the 2D perovskite domains extend nearly 20 to 30 nm from the film surface into the bulk. Locally averaged EDP from the regions marked in yellow and red boxes in Fig. 3A are shown in Fig. 3 B and C, respectively. The primary reflections corresponding to the 3D and 2D perovskite lattice planes are marked accordingly. The {110} reflections of the 3D MAPbI$_3$ perovskite, which have been notoriously hard to find, are detected under our NBED measurement conditions in single (millisecond exposure) patterns, i.e., with ultralow electron fluence, notwithstanding the weak interaction of these planes with the incident e-beam (21). Notably, the diffraction pattern in Fig. 3C shows the presence of phase-pure $n = 1$ FPEA$_2$PbI$_4$, with higher-order reflections clearly visible along with the basal plane reflections, unequivocal evidence for long-range ordering in the 2D perovskite. The rotation of the diffraction patterns relative to the scan coordinates is compensated in Fig. 3 such that the directions in real and reciprocal space coincide. In agreement with the XRD data (Fig. 1) that show (00l)-preferred 2D orientation, the EDPs show that the 2D layers are oriented horizontally, meaning that the (PbI$_6$)$^-$ octahedra are arranged nearly parallel with respect to the substrate surface plane. Such an orientation is preferred if ultrathin 2D layers are to protect 3D HaPs from ambient, especially moisture, to improve 3D stability. This indicates that the controlled vapor phase conversion of 3D into 2D perovskite phases that we
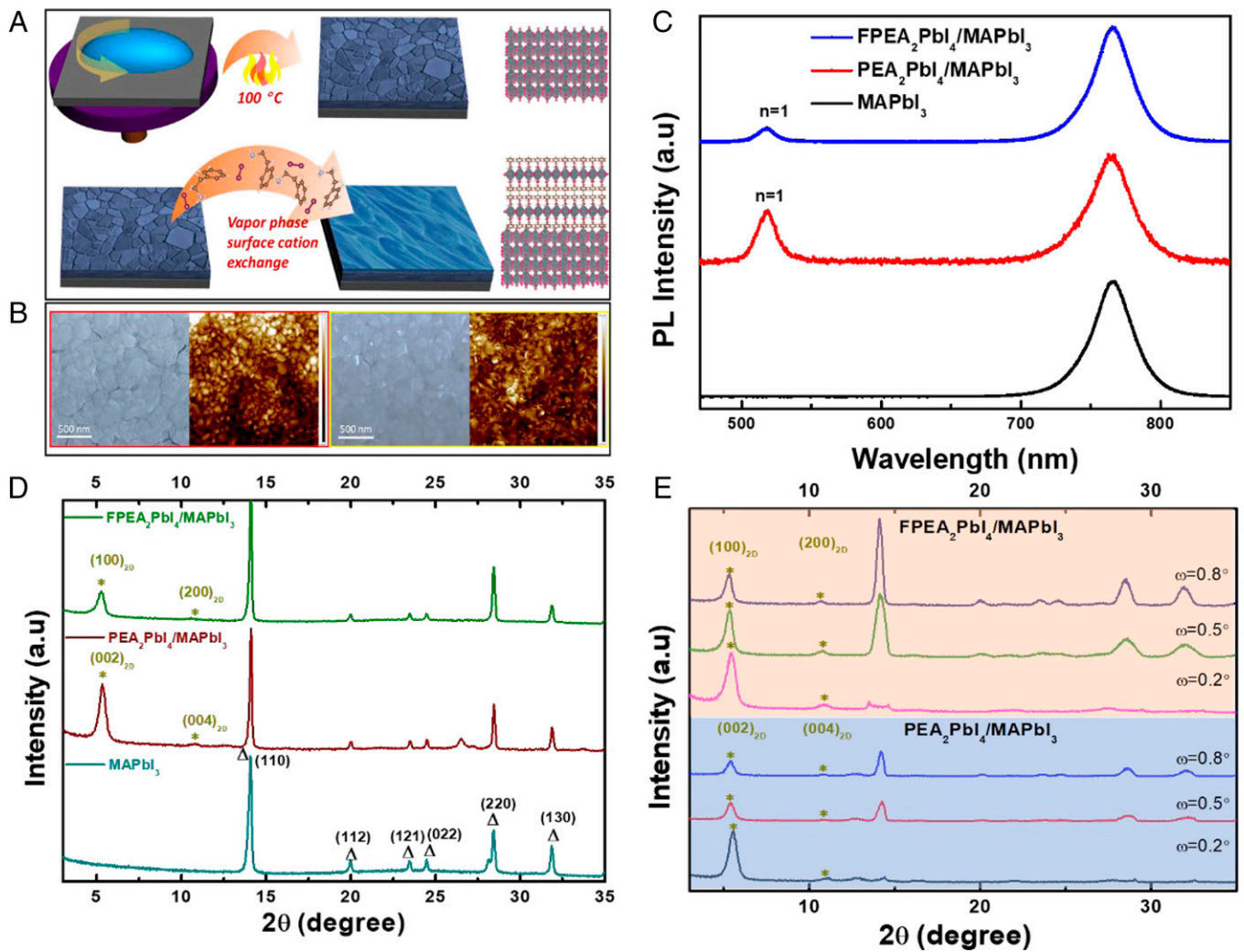
Kumar et al.
Halide perovskite dynamics at work: Large cations at 2D-on-3D interfaces are mobile

PNAS | 3 of 9
https://doi.org/10.1073/pnas.2114740119

Fig. 1. (*A*) Schematic representation 2D/3D HaP layer formation via vapor phase surface cation exchange method. (*B*) Images show representative SEM and atomic force microscopy (AFM) (2 μm × 2 μm) images of the 3D and 2D/3D films. (*C*) PL emission data of the 3D and 2D/3D perovskite layers collected from the top side (side exposed to the vapor with large cation precursor) of the layers. (*D*) Bragg-Brentano and (*E*) grazing incidence XRD of the 2D/3D perovskite layers. a.u. is arbitrary unit.

employed is a viable way to make ultrathin, phase-pure 2D perovskite layers on top of their 3D counterparts.

2D HaP in the 3D Matrix. Remarkably, in another 2D/3D/Si lamella (Fig. 4*A*), freshly prepared and measured under the same conditions, a 2D perovskite domain was found 70 to 80 nm away from the HaP interface with the carbon coat, apparently within the 3D matrix, during the first TEM scan. The angular correlation map for the lattice period of 0.6 nm^{-1} is shown in Fig. 4*B* and clearly indicates that this domain is 2D material. For clarity, the area within the dashed lines in Fig. 4*A* shows the subfilm surface location of the 2D n = 1 domain in the virtual bright-field image. This 2D area is without cracks or holes, well-removed from the interface with C coating, which might have allowed some sort of impregnation by the top 2D capping layer. Thus, we conclude that the 2D domain that apparently is within the 3D matrix (see later) is not a result of sample preparation or a measurement-induced artifact.

The EDPs from the regions marked by yellow and red ovals in Fig. 4*B* in the 2D perovskite region at the top of the sample (at the contact with the carbon coating) and the 2D domain away from the HaP interface with the carbon coat are shown in Fig. 4 *C* and *D*, respectively. As noted earlier (discussion of

Fig. 3), the diffraction patterns have been compensated for the rotation between diffraction and image plane in the TEM to yield the same directions in real and reciprocal space. The 2D perovskite structures at the surface with the ambient (the open surface) (Fig. 4*C*) have their (00*l*) planes more parallel to the substrate plane than is the case for the 2D domain, apparently within the 3D HaP domain, which are more perpendicular to the substrate plane (Fig. 4*D*). Such an alternative orientation of the 2D structures with planes perpendicular to the substrate surface will be (more) prone to degradation because of ambient species diffusion through the van der Waal's gaps between adjacent organic moieties.

What can be the nature/origin of the possible, and, in view of Fig. 4*B* likely, interdiffusion process? To answer this question, we mapped the 3D HaP grains in and around the 2D phase within the 3D HaP according to their lattice spacings, as shown in green and blue in the angular correlation RGB (red-green-blue) map (*SI Appendix*, Fig. S5*A*). The red in the map shows a 2D n = 1 phase, the same as in Fig. 4*B*. We recall that in Fig. 4*A*, no cracks/holes that could be filled by the 2D capping layer are seen at and around that region. Further analysis, using the angular correlation RGB map (*SI Appendix*, Fig. S5*A*) shows that the 2D domain inside the HaP matrix lies at a saddle-point
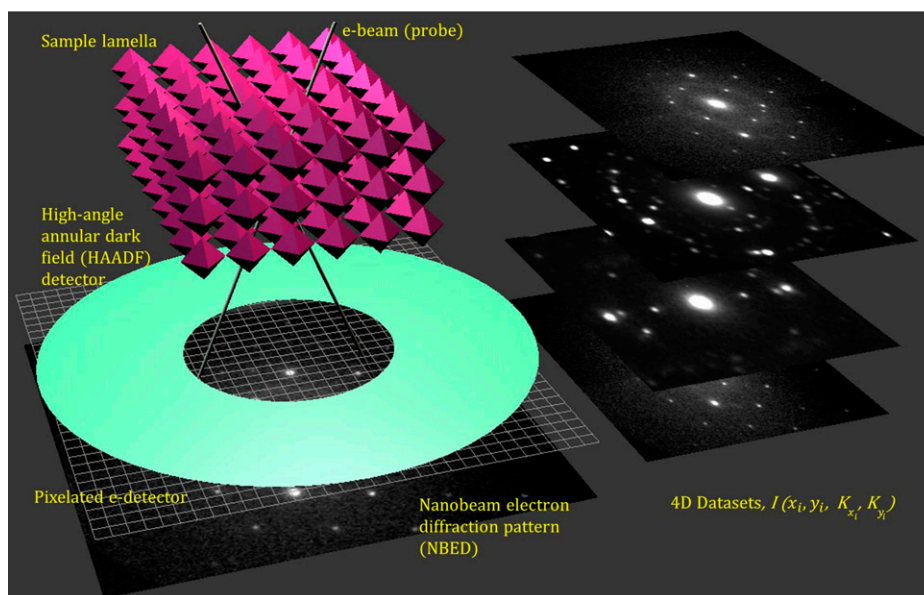
Fig. 2. Schematic representation of a typical 4D STEM experiment. A STEM probe rasters over the sample and the pixelated electron detector records the diffraction pattern for each probe position on the raster grid. The convergence angle of the STEM probe used was $\lesssim 0.2$ mrad, which resulted in probe sizes in the range from a few nanometers to a few tens of nanometers. For illustration, four representative EDPs, out of a few tens of thousands of EDPs in a typical 4D dataset, are shown.

intersection of two 3D grains, around a grain boundary that runs from the Si/HaP interface to the 2D surface-capping layer. The STEM bright-field image (*SI Appendix*, Fig. S5*B*) shows a grain boundary at a location that matches that of the 2D domain in the 3D HaP matrix. Grain boundaries can often serve as diffusion shortcuts, and in polycrystalline HaP films as in this case (and thus also in HaP-based photovoltaic devices with 2D/3D bilayer configuration), they can promote fast in- or interdiffusion of organic amines/ammonium cations. Hence, they can affect 2D or quasi-2D phase distribution in the 3D HaP matrix. Note that the STEM bright-field image (*SI Appendix*, Fig. S5*B*) confirms the absence of cracks or voids that could be filled by the 2D capping layer to explain the domain inside the HaP film.

To understand the crystallographic phase nature of this 2D domain, we show the EDPs (Fig. 5 *A–H*) across the 2D phase within the 3D one sequentially along the green-colored arrow marked across the red oval in the angular correlation map (Fig. 4*B*). The EDPs show a gradual structural transition from 3D HaP reflections, visible in Fig. 5*A*, followed by reflections corresponding to the 2D HaP phase appearing in Fig. 5*B* along with the 3D reflections. The reflections in the EDPs shown in Fig. 5 *C–F*, which are from the region within the 2D perovskite domain, reveal the $n = 2$ (labeled in yellow) 2D phase along with the pure 2D phase ($n = 1$, labeled in white) that was originally deposited on the 3D HaP film. Proceeding toward the film surface along the arrow, the $n = 1$ 2D perovskite reflection disappears, while the remaining extra (to the 3D HaP) reflections might indicate the formation of $n = 3$ 2D perovskite phases near the surface (Fig. 5 *G* and *H*) after the possible interdiffusion.

These results indicate that the origin of this 2D HaP structure (away from the HaP/carbon coat interface) is different from the one that we find in the 2D regions near/at the open film surface. The difference in orientation and the formation of quasi-2D phases near the surface region can be related to how these regions form. The different orientation can be understood from the presence of this 2D patch at a saddle-point intersection between grains, along the boundary between the

grains. As such, its formation testifies to the dynamics of interdiffusion that leads to the 2D/3D interfaces at the edges of the patch.

Based on these results we propose that part of the original 2D perovskite, i.e., the large 2D cations, migrates along grain boundaries into the 3D HaP film; in doing so, $n = 1$ 2D/3D HaP interfaces reconstruct into $n = 1$ appearing inside the 3D matrix and $n > 1$ 2D/3D phases near the surface region. These processes would occur in a polycrystalline 3D HaP films in addition to the in-diffusion of the 2D cations into the 3D matrix through the free surfaces. This implies that such 2D/3D perovskite heterointerface lattice rearrangements involve migration of not only (the smaller) MA^+ but also of the larger $FPEA^+$ cation into the 3D matrix and, likely faster, along the grain surfaces and boundaries. Indications for such were seen also in experiments with $PEA_2PbI_4/MAPbI_3/FTO$ samples, in which 2D perovskite domains were also found within the 3D perovskite, including some even near the bottom interface with FTO (*SI Appendix*, Fig. S4*D*). However, in that case we cannot rule out that these changes were related also to the sample degradation seen on FTO substrates. Nevertheless, these results directly show the effect of 2D/3D interface dynamics, as was inferred till now from PL and XRD data.

We also show evidence from the PL measurements for formation of such quasi-2D phases in these 2D/3D HaP films under different ex situ exposure conditions (*SI Appendix*, Fig. S6). The results of these measurements corroborate our TEM findings on the local dynamical processes that occur at the interfaces of 2D-on-3D perovskite layers. Furthermore, the results show that the 3D HaP interfaces made with PEA-based 2D layers show $\sim\!\!>\!2\times$ faster occurrence of such processes, as deduced from appearance of quasi-2D phases, than interfaces formed with monosubstituted fluorinated (F-PEA) analogs.

The possibility of 2D cations diffusing into the 3D perovskite lattice without being mediated by external factors (apart from weak room light and kT, for room temperature) was investigated on a diced portion of the same $FPEA_2PbI_4/MAPbI_3/Si$ sample, the results of which are shown in Fig. 4. Contrary to the previous experiment, in this case the samples were

Kumar et al.
Halide perovskite dynamics at work: Large cations at 2D-on-3D interfaces are mobile

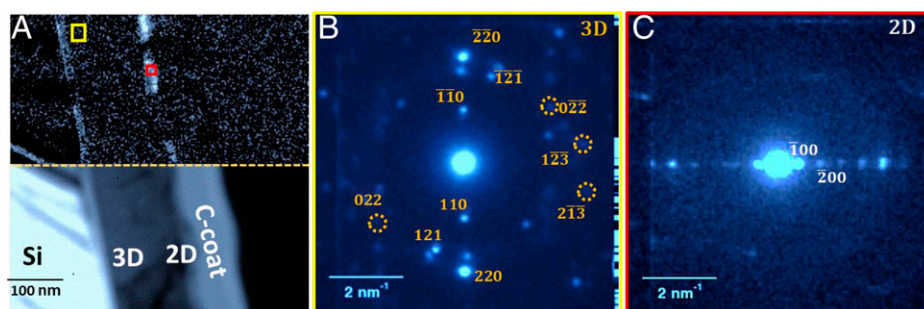PNAS | 5 of 9
https://doi.org/10.1073/pnas.2114740119

Fig. 3. (*A*) Bright-field STEM image (*Lower*) and the angular correlation map for the 2D basal plane reflections (*Upper*). The two images are matched suitably for assisting the visual comparison of the different layers. (*B*) and (*C*) show the EDPs collected from the region marked in *A*. The EDPs have been rotated fittingly to match the scan coordinate system in the real space. C-coat refers to the protective carbon coating grown on top of the 2D/3D heterostructure prior to FIB lamella preparation.

completely sealed and stored in a dry N_2-filled glovebox for >2 mo. FIB lamellae were prepared from these samples under the same conditions as before.

As shown in Fig. 6, we could observe a clear contrast in the angular correlation maps for the 2D perovskite base period of 0.6 nm^{-1} of the fresh and 2-mo–stored 2D/3D samples. The pure 2D, $n = 1$ phase is mostly absent in the region adjacent to the carbon interface, and a segregated ~60 nm 2D phase is observed for the latter, while it is unequivocally present within ~20 nm from the interface for the fresh samples, excluding the domain that has supposedly migrated into the 3D region following some external stimulus. Furthermore, the EDPs from such a 2D perovskite region in Fig. 6*B* indicate the signatures for the presence of 2D HaP material with $n > 1$ alongside the $n = 1$ 2D phase, which are not observed in freshly prepared samples (Figs. 3*C* and 4*B* marked within yellow oval).
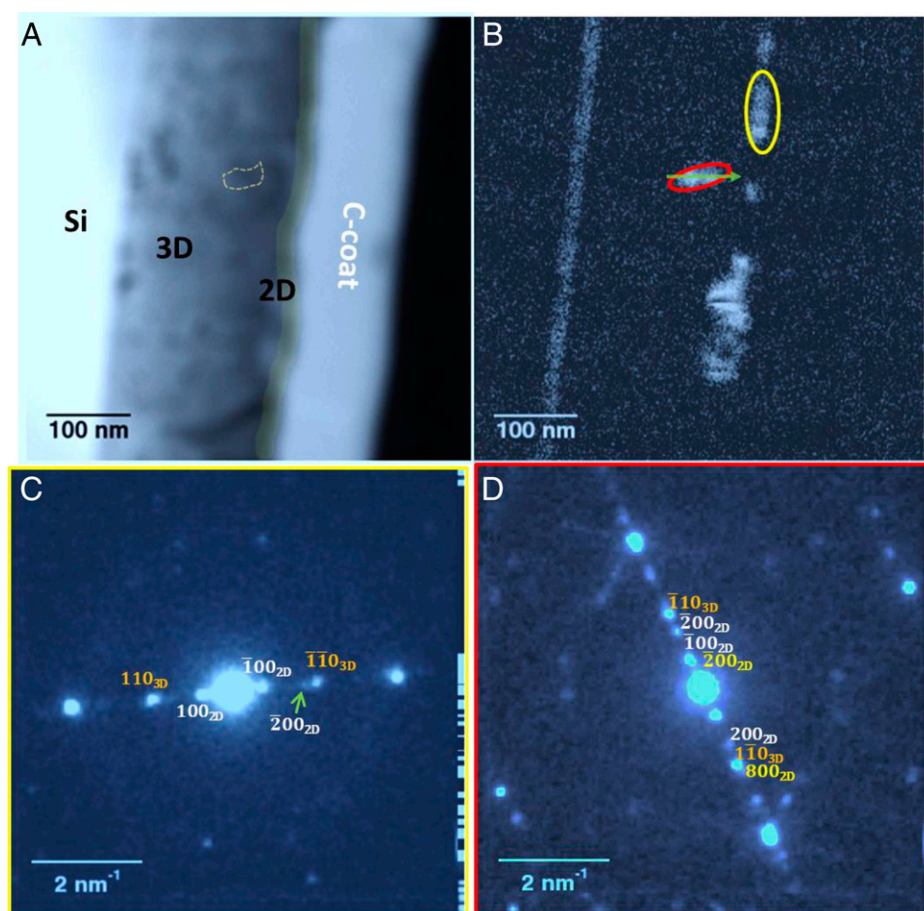

Fig. 4. 4D STEM dataset revealing transformation of the 2D/3D HaP layers, with 2D signatures appearing deep inside the film. (*A*) Virtual bright-field image. The different layers are marked. Contrast variations in the perovskite film are related to Bragg diffraction by crystalline grains. (*B*) Angular correlation map for 2D ($n = 1$) basal plane reflections (0.6 nm^{-1}), tell-tale proof of the 2D crystal symmetry (cf. subsection *4D-STEM at low electron fluence* in the text); *C* and *D* show the EDPs collected from the red and yellow ovals marked in *B*, in which white and yellow indicate $n = 1$ and $n = 2$ reflections, respectively. {110} 3D reflections are indicated in ochre color. The ED patterns are rotated to have identical real-space TEM image planes for both patterns. C-coat refers to the protective carbon coating grown on top of the 2D/3D heterostructure prior to FIB lamella preparation.
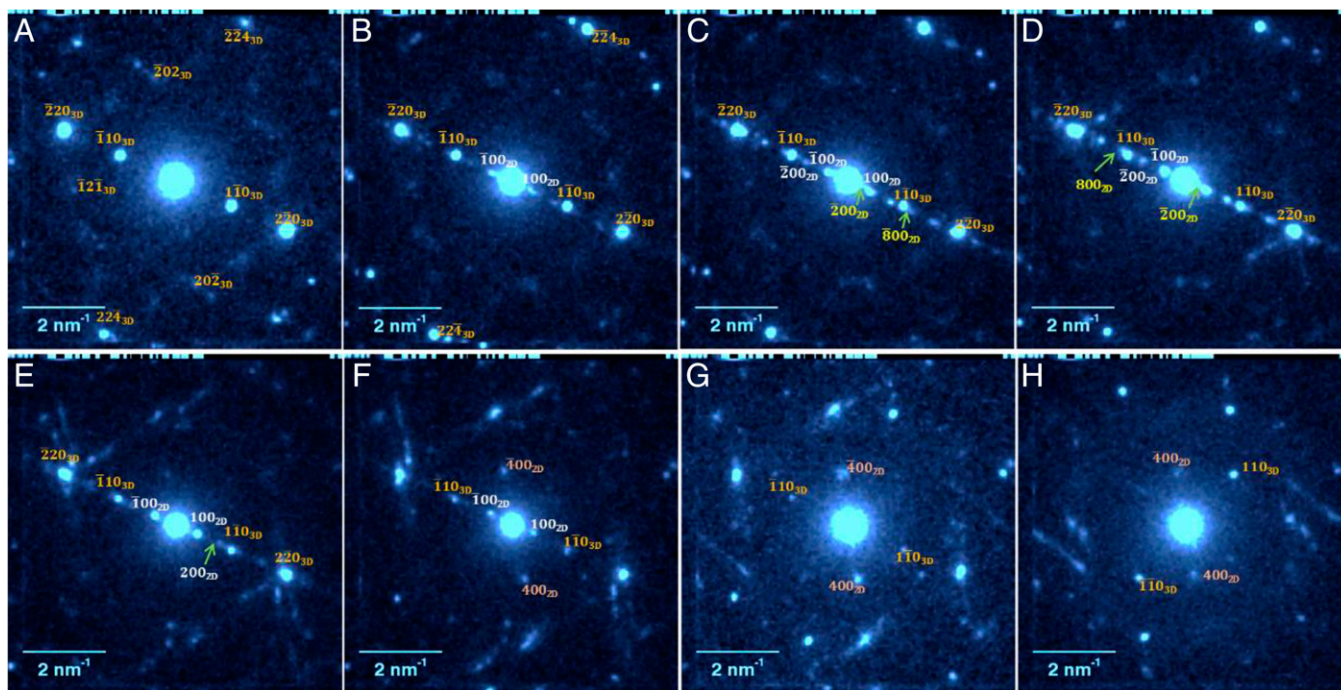
Fig. 5. (*A*–*H*) EDPs across the 2D perovskite phase away from the nominal 2D/3D interface (within the red oval, shown in the angular correlation map shown in Fig. 4*B*) are shown sequentially along the arrow (marked in Fig. 4*B*) toward the surface of the sample (i.e., toward the C-coat).

Structure Evolution under the Electron Beam. To elucidate the evolution of the 2D/3D HaPs and their interfaces directly under the electron beam as external degrading factor, we recorded a time series (*SI Appendix*, Figs. S8 and S10 and Movies S2 and S3) of the EDP evolution under continuous e-beam irradiation (with low electron fluence ~2 e/Å^2 per millisecond frame time) from the 2D and 3D HaP regions in the lamella. The structural instability of the 2D phase is remarkably more pronounced under e-beam exposure: The higher-order reflections vanish within just 60 to 80 ms of exposure, implying the loss of long-range ordering in the 2D perovskite domains. These structural instabilities due to e-beam exposure could be typical for these (Ruddlesden-Popper) layered structures held together by weak van der Waals interactions. This can be compared to the chemically less labile 3D MAPbI$_3$ structures, even though their lability under e-beam irradiation is well documented, but under harsher e-beam conditions (22).

We found no noticeable change in 3D perovskite reflections even with orders of magnitude higher fluence than what is considered the limit for damage, a feature we ascribe to the very narrow beam used. The apparently surprising sample resilience

to electron beam damage is found in the experiment in which we use an e-fluence at a 2 e/Å^2/ms rate during a few seconds on the sample, i.e., several thousands of e/Å^2, clearly much higher than the critical fluence, 50 e/Å^2, reported in the literature (22, 29). To understand this result, it should be realized that our conditions for 4D STEM NBED data collection are fundamentally different from those for the more usual, selected area diffraction (SAED) pattern mode. In 4D STEM, the beam diameter is at most a few tens of nanometers, which can be compared to several microns for SAED (22). Hence, the excess deposited energy in the 4D STEM experiment is very localized and will diffuse readily across and into the sample to the surroundings, leading to much reduced background heating compared to what is the case for SAED. This lower heating strongly reduces any deleterious thermal effects on the sample during and after the measurement. With SAED, the wider e-beam leads to drastic sample degradation already at close to 100× lower total electron fluences (≤~50 e/Å^2) than the thousands of e/Å^2 that can be tolerated under our 4D STEM NBED experimental conditions (22). In addition, the unintentional parasitic coating of the FIB lamella with redeposited carbon
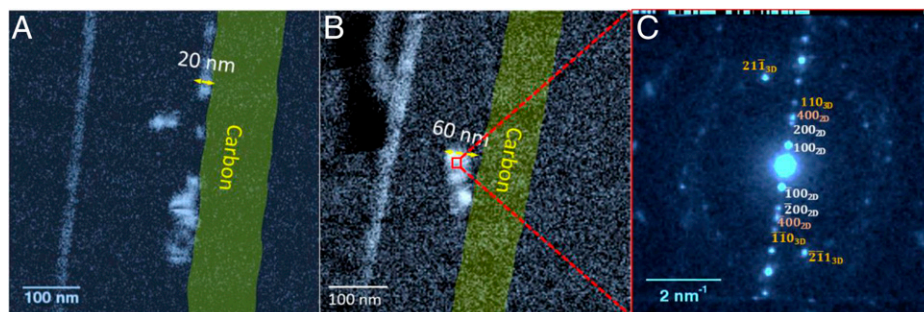

Fig. 6. Angular correlation maps (*A* and *B*) corresponding to the 2D basal plane (100) reflections of FPEA$_2$PbI$_4$ which show the locations of the 2D phase in a freshly prepared sample (*A*) and that of a sample stored in a completely sealed, air-free N$_2$ glovebox for over 2 mo (*B*). Fig. 4*B* is here shown again, as *A*, to allow direct visual comparison of distance of the 2D region from the HaP/C-coat interface in *A* and *B*. (*C*) shows the EDP from the 2D region marked in *B*, with reflections corresponding to a higher *n*, i.e., 2D/3D perovskite phase, along with those of the *n* = 1 2D perovskite phase.
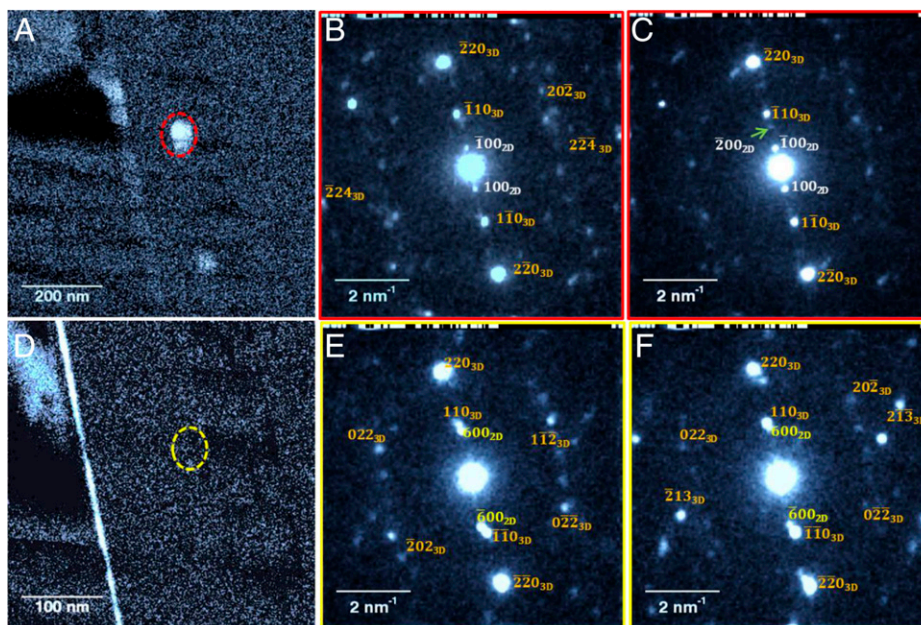
Kumar et al.
Halide perovskite dynamics at work: Large cations at 2D-on-3D interfaces are mobile

PNAS | 7 of 9
https://doi.org/10.1073/pnas.2114740119

Fig. 7. Angular correlation maps (*A* and *D*) for the 2D perovskite base period under repetitive e-beam scan of the same region in an FPEA$_2$PbI$_4$/MAPbI$_3$/Si sample. (*A*) and (*D*) show the data recorded in the first and third acquisition, respectively. (*B*) and (*C*) and (*E*) and (*F*) are the corresponding EDPs recorded from two representative spots within the region marked in red and yellow oval in *A* and *D*, respectively, showing the structural evolution after the repetitive e-beam exposures.

may have also helped in reducing the beam damage and increasing the critical fluence, as this coating can serve as a diffusion barrier and reduce the escape probability of the volatile species. Such an effect was demonstrated by Chen et al. for a carbon-coated MAPbI$_3$ specimen deposited on a holey carbon copper grid (37).

The dynamic structural evolution at these 2D/3D heterointerfaces under the e-beam is further studied by recording the electron diffraction maps under repetitive e-beam scans (with a fluence of ~5 e/Å^2 per scan) over a region of the lamella that includes these 2D/3D interfaces. The angular correlation maps for the 2D perovskite ($n = 1$) phase between the first and third scan are compared in Fig. 7 *A* and *D*. The bright domains in the maps, which show the 2D HaP, effectively disappear as the result of the repetitive e-beam exposures, i.e., after a total electron fluence of ~15 e/Å^2 irradiated on the 2D/3D HaP lamella. The EDPs of these regions of interest are contrasted in Fig. 7 *B* and *C* versus *E* and *F*, where Fig. 7 *B* and *C* and Fig. 7 *E* and *F* show the diffraction patterns from different regions marked in red and yellow ovals of the same sample after the first and third scans, respectively. Notably, reflections that can be attributed to the $n = 2$ 2D phase (labeled in yellow in Fig. 7 *E* and *F*) can be discernible along with the 3D MAPbI$_3$ reflections after the loss of 2D ($n = 1$) reflections in the third successive scan. Sequential e-beam scans, while capturing lattice information from each probe position on the lamella, also increase the cumulative electron fluence deposited at those probe positions, possibly mimicking the effect of other external factors on such a HaP system, e.g., temperature. We note that the time constant for a single scan position in our experiments is 1 ms, with frame repetition rates in the order of 1 min; hence, we cannot rule out or confirm for the effects of the temporal processes like sample relaxation and recovery processes (after the electron impact) on the structural response of the 2D/3D HaP interfaces (23). However, the energy imparted by the e-beam seems to have reconstructed the pristine 2D/3D interfaces into $n = (>)2$ 2D/3D phases inside the 3D matrix. This suggests that the $n > 1$ 2D/3D HaP is more stable against e-beam–induced damage than the $n = 1$ 2D one.

Summary. Atomic-scale investigations on beam-sensitive materials such as the 3D HaPs and the interfaces that they form with their low-dimensional analogs require specialized techniques and analyses, unlike what works for more robust (inorganic) materials, for which the material–e-beam interaction does not alter their structures so readily.

NBED experiments, performed with ultralow electron doses, allowed us to observe the often overlooked (110) reflections for tetragonal MAPbI$_3$, the absence of which in HaP TEM studies, should be a warning sign. Under prolonged/repetitive e-beam exposure, the 2D material loses long-range ordering in <100 ms of low-dose e-beam fluence, which provides another limit on use of TEM to study these materials. Having determined the onset of instability, we could then obtain crucial atomic-scale insights into 2D/3D HaPs interface, showcasing the inherent dynamic instability of those we studied. Such an unstable interface can manifest itself in the change of device performance with (short) time, as shown recently with improved PCEs after suggested formation of quasi-2D material at the interface (11). It remains to be seen if such a phenomenon can cause additional, possibly negative effects in the long run.

The spatial migration of the large 2D-forming cations into the 3D HaP matrix from and via the free surfaces, and likely faster along grain boundaries, and the appearance of 2D phases with $n > 1$ around a grain boundary near the surface region and over time imply that both the smaller MA$^+$ and the longer F-PEA$^+$ cations can migrate, leading to lattice rearrangements. Understanding such instabilities will be critical for avoiding (inter)diffusion of A-site cations in lead iodide–based HaPs and the structural consequences of such diffusions. Apart from the above-mentioned long-term stability issue, our results pose a challenge in understanding the structural and energetic aspects of diffusion of the relatively large F-PEA$^+$ cation into and through the 3D HaP matrix. Most importantly, at least for the direction of research that stimulated this study, our results point to the need for more sophisticated design of 2D HaPs if they are to be used as protective barriers for 3D HaP–based photovoltaic devices.

1. K. Teshima, M. Suzuki, Y. Shirai, M. Rikukawa, K. Sanui, Preparation and optical characterizations of optically active quantum well films consisting of organic-inorganic layered perovskite compounds. Japanese J. Appl. *Physics, Part 2 Lett* **42**, 11–14 (2003).
2. C. C. Stoumpos *et al.*, Ruddlesden-Popper hybrid lead iodide perovskite 2D homologous semiconductors. *Chem. Mater.* **28**, 2852–2867 (2016).
3. D. H. Cao, C. C. Stoumpos, O. K. Farha, J. T. Hupp, M. G. Kanatzidis, 2D homologous perovskites as light-absorbing materials for solar cell applications. *J. Am. Chem. Soc.* **137**, 7843–7850 (2015).
4. D. Wang, M. Wright, N. K. Elumalai, A. Uddin, Stability of perovskite solar cells. *Sol. Energy Mater. Sol. Cells* **147**, 255–275 (2016).
5. W. Fu, H. Chen, A. K. Y. Jen, Two-dimensional perovskites for photovoltaics. *Mater. Today Nano.* **14**, 100117 (2021).
6. M. S. Abbas *et al.*, Orientationally engineered 2D/3D perovskite for high efficiency solar cells. *Sustain. Energy Fuels* **4**, 324–330 (2019).
7. H. Tsai *et al.*, High-efficiency two-dimensional Ruddlesden-Popper perovskite solar cells. *Nature* **536**, 312–316 (2016).
8. J. Chen, J. Y. Seo, N. G. Park, Simultaneous improvement of photovoltaic performance and stability by in situ formation of 2D perovskite at (FAPbI3)0.88(CsPbBr3)0.12/CuSCN interface. *Adv. Energy Mater.* **8**, 1702714 (2018).
9. V. E. Madhavan *et al.*, CuSCN as hole transport material with 3D/2D perovskite solar cells. *ACS Appl. Energy Mater.* **3**, 114–121 (2020).
10. Y. Liu *et al.*, Ultrahydrophobic 3D/2D fluoroarene bilayer-based water-resistant perovskite solar cells with efficiencies exceeding 22. *Sci. Adv.* **5**, eaaw2543 (2019).
11. A. A. Sutanto *et al.*, Dynamical evolution of the 2D/3D interface: A hidden driver behind perovskite solar cell instability. *J. Mater. Chem. A Mater. Energy Sustain.* **8**, 2343–2348 (2020).
12. Z. Liu *et al.*, In situ observation of vapor-assisted 2D-3D heterostructure formation for stable and efficient perovskite solar cells. *Nano Lett.* **20**, 1296–1304 (2020).
13. Y. Lin *et al.*, Enhanced thermal stability in perovskite solar cells by assembling 2D/3D stacking structures. *J. Phys. Chem. Lett.* **9**, 654–658 (2018).
14. A. A. Sutanto *et al.*, In situ analysis reveals the role of 2D perovskite in preventing thermal-induced degradation in 2D/3D perovskite interfaces. *Nano Lett.* **20**, 3992–3998 (2020).
15. K. Song *et al.*, Atomic-resolution imaging of halide perovskites using electron microscopy. *Adv. Energy Mater.* **10**, 1–15 (2020).
16. Y. Zhou, H. Sternlicht, N. P. Padture, Transmission electron microscopy of halide perovskite materials and devices. *Joule* **3**, 641–661 (2019).
17. T. W. Jones *et al.*, Lattice strain causes non-radiative losses in halide perovskites. *Energy Environ. Sci.* **12**, 596–606 (2019).
18. M. Long *et al.*, Textured CH3NH3PbI3 thin film with enhanced stability for high performance perovskite solar cells. *Nano Energy* **33**, 485–496 (2017).
19. F. Zhu *et al.*, Shape evolution and single particle luminescence of organometal halide perovskite nanocrystals. *ACS Nano* **9**, 2948–2959 (2015).
20. L. Gao *et al.*, Passivated single-crystalline CH$_3$NH$_3$PbI$_3$ nanowire photodetector with high detectivity and polarization sensitivity. *Nano Lett.* **16**, 7446–7454 (2016).
21. T. W. Kim *et al.*, Self-organized superlattice and phase coexistence inside thin film organometal halide perovskite. *Adv. Mater.* **30**, 1–8 (2018).
22. S. Chen *et al.*, Atomic scale insights into structure instability and decomposition pathway of methylammonium lead iodide perovskite. *Nat. Commun.* **9**, 4807 (2018).
23. E. J. VandenBussche, C. P. Clark, R. J. Holmes, D. J. Flannigan, Mitigating damage to hybrid perovskites using pulsed-beam TEM. *ACS Omega* **5**, 31867–31871 (2020).
24. D. Zhang *et al.*, Atomic-resolution transmission electron microscopy of electron beam–sensitive crystalline materials. *Science* **359**, 675–679 (2018).
25. Y. Yan *et al.*, Benefiting from spontaneously generated 2D/3D bulk-heterojunctions in Ruddlesden-Popper perovskite by incorporation of S-bearing spacer cation. *Adv. Sci. (Weinh.)* **6**, 1900548 (2019).
26. J. W. Lee *et al.*, 2D perovskite stabilized phase-pure formamidinium perovskite solar cells. *Nat. Commun.* **9**, 3021 (2018).
27. M. U. Rothmann *et al.*, Structural and chemical changes to CH$_3$ NH$_3$ PbI$_3$ induced by electron and gallium ion beams. *Adv. Mater.* **30**, e1800629 (2018).
28. R. F. Egerton, Control of radiation damage in the TEM. *Ultramicroscopy* **127**, 100–108 (2013).
29. M. U. Rothmann *et al.*, Atomic-scale microstructure of metal halide perovskite. *Science* **370**, eabb5940 (2020).
30. R. M. Kennard *et al.*, Phase stability and diffusion in lateral heterostructures of methyl ammonium lead halide perovskites. *ACS Appl. Mater. Interfaces* **11**, 25313–25321 (2019).
31. M. Kuno, M. C. Brennan, What exactly causes light-induced halide segregation in mixed-halide perovskites? *Matter* **2**, 21–23 (2020).
32. C. Ophus, Four-dimensional scanning transmission electron microscopy (4D-STEM): From scanning nanodiffraction to ptychography and beyond. *Microsc. Microanal.* **25**, 563–582 (2019).
33. M. W. Tate *et al.*, High dynamic range pixel array detector for scanning transmission electron microscopy. *Microsc. Microanal.* **22**, 237–249 (2016).
34. Q. Zhou *et al.*, High-performance perovskite solar cells with enhanced environmental stability based on a (p-FC 6 H 4 C 2 H 4 NH 3) 2 [PbI 4] capping layer. *Adv. Energy Mater.* **9**, 1802595 (2019).
35. D. H. Olson *et al.*, Size effects on the cross-plane thermal conductivity of transparent conducting indium tin oxide and fluorine tin oxide thin films. *IEEE Trans. Components, Packag. Manuf. Technol.* **9**, 51–57 (2019).
36. M. Asheghi, K. Kurabayashi, R. Kasnavi, K. E. Goodson, Thermal conduction in doped single-crystal silicon films. *J. Appl. Phys.* **91**, 5079–5088 (2002).
37. S. Chen *et al.*, General decomposition pathway of organic-inorganic hybrid perovskites through an intermediate superstructure and its suppression mechanism. *Adv. Mater.* **32**, e2001107 (2020).

APPLIED PHYSICAL SCIENCES

Kumar et al.
Halide perovskite dynamics at work: Large cations at 2D-on-3D interfaces are mobile

PNAS | 9 of 9
https://doi.org/10.1073/pnas.2114740119